Preliminary Viability Assessment of Cislunar Periodic Orbits for Space Domain Awareness

Adam P. Wilmer, Robert A. Bettinger, and Bryan D. Little
Air Force Institute of Technology, Wright-Patterson Air Force Base, OH

ABSTRACT

Performing Space Domain Awareness (SDA) utilizing classical terrestrial and/or space-based sensors in near-Earth space becomes increasingly difficult when applied to the cislunar orbit regime. Therefore, cislunar periodic orbits are presented as a means to fill this capability gap. While there are many uses for periodic orbits, this work assesses the effectiveness of various Earth-Moon periodic orbits in a sample SDA mission architecture. Specifically, several different types of periodic orbits within cislunar space are modeled in order to evaluate their respective effectiveness in tracking/monitoring two notional satellites evenly spaced in a Lyapunov orbit about the L1 Lagrange point. The orbits analyzed are modeled in the circular restricted three-body problem (CR3BP). The propellant required to maintain the same trajectory when transitioning to the bicircular restricted four-body problem (BCR4BP) is also presented. The implementation of multiple dynamical models is sought in order to compare orbit maintenance costs when transitioning to higher fidelity models such as from the CR3BP to the BCR4BP. Notional space-to-space sensors are used to determine limitations of periodic orbit geometry for the SDA mission as a function of range, capability, and Sun/Earth/Moon exclusion angles. Visual magnitude is used in determining if a target is visible. Tabulated results of the findings are presented with recommendations for the most effective periodic orbit for cislunar SDA.

1. INTRODUCTION

The opening decades of the twenty-first century witnessed a reemergence of international attention towards the realization of space missions into the cislunar environment and beyond, with both nations and private companies investigating the formation of missions to the Moon and Mars. With national plans to create a Lunar Gateway orbiting the Moon, develop a long-term human presence on the Moon, and facilitate preparations for Human missions to Mars via NASA's Artemis program, the United States has a vested interest in exploring trajectory design within multi-body gravitational systems. One such class of trajectories, identified herein as cislunar periodic orbits, could provide a reliable astrodynamical means of supporting missions such as re-supply, personnel transport, and space-based infrastructure development. With increasing missions beyond near-Earth orbit, the use of a subset of these periodic orbits for space domain awareness (SDA) mission architectures may also prove beneficial for the timely identification and tracking of resident space objects, such as satellites or space debris, to ensure safe space traffic management. A recent study was published [4] which investigated the use of Earth-Moon 2:1 periodic resonant orbits for SDA.

When compared with alternative types of orbital trajectories, periodic orbits provide mission-related benefits in terms of propellant savings for orbit maintenance. This is the result of periodic orbits designed to repeatedly traverse a given region of the toroidal volume of cislunar space with a lower propellant expenditure than typical non-periodic cislunar trajectories. Multiple types of periodic orbits will be investigated for their effectiveness in performing an SDA mission with respect to two notional resident spacecraft in a Lyapunov orbit about the Earth-Moon L1 Lagrange point. The initial conditions required for these periodic orbits are found using previous work from Arenstorf [1, 2] who used a dated non-dimensional mass parameter, μ, in his Circular Restricted Three-Body Problem (CR3BP) analysis, therefore, differential correction is used to normalize these orbits to a modern non-dimensional mass parameter.

Propellant expenditure is a dominant cost which determines the lifespan of a given spacecraft system. The periodic orbits analyzed in this work have the ability to repeat their orbital trajectory for months with no additional propellant in the CR3BP. However, chaos is introduced in the system with the added perturbation of the Sun's gravitational force as seen in the Bicircular Restricted Four-Body Problem (BCR4BP). The computation of orbit maintenance costs for each periodic orbit in the BCR4BP will be made to show the low propellant required for these orbits in higher fidelity models. The factors that are analyzed for determining periodic orbit effectiveness are: SDA coverage, propellant costs in the BCR4BP, and period (i.e., revisit time). For SDA coverage, each variety of periodic orbit will host a

sensor bearing satellite constellation consisting of 10 satellites evenly space in time across the orbit monitoring 2 notional satellites, identified herein as "Targets", in an L1 Lyapunov orbit. Notional space-to-space sensors are used to determine limitations of periodic orbit geometry for the SDA mission as a function of sensor range, capability, and gravitational body exclusion angles. Tabulated results of the findings will be presented with recommendations for which periodic orbit is most effective for this cislunar SDA mission architecture.

2. BACKGROUND

In the late 19th century, Poincaré [9] made considerable contributions in the qualitative theory of the restricted three-body problem and dynamical systems alike. His work was the first to hint at the chaotic behavior of a dynamical system and inevitably proved that the CR3BP solution is infinitely discontinuous. While director of the Copenhagen Observatory, Strömgrén led his team to numerically determine and categorize families of periodic orbits; the tabulated results were published in 1934 [11].

In 1958, Egorov [3], unsatisfied with the solutions which literature of the time provided, noted many questions were either left unanswered or not fully answered with respect to periodic resonant orbits. These questions pertained to possible trajectories for circumnavigating the Moon and returning to Earth, the shape and classification of trajectories in the passive phase, the problem of minimum initial velocities required for reaching the moon, and the effect produced by a spread in the initial conditions on the characteristics of various lunar flight trajectories. An evolution in computing technology around this time was pivotal in accelerating progress in the field of trajectory design with numerical integration significantly more feasible, thus leading to more discoveries of periodic solutions [12].

In the early 1960's, Arenstorf [1, 2] presented methods for solving families of synodically-closed periodic solutions in the CR3BP which, he noted, can be altered to have close proximity passes to both gravitational primaries. These periodic orbits are presented in terms of resonance, order, and period. In 1967 Szebehely [12] synthesized his knowledge of dynamics and the three body problem to culminate one of the first books on the subject: *Theory of Orbits*. This work provided a standard knowledge base and created a fundamental structure for how academicians may study the restricted problem of three bodies.

Overall, the majority of research since the mid-twentieth century pertaining to periodic orbits within a multi-body gravitational system has focused on the determination of trajectory solutions for symmetric periodic orbits. A segment of researchers embarked on describing and determining families of asymmetric solutions, with such analysis requiring two initial values to be simultaneously adjusted in order to obtain a periodic solution as opposed to one with symmetric orbits [7]. This work focuses on the analysis of SDA along symmetric periodic orbits.

3. METHODOLOGY

3.1 Circular Restricted Three-Body Problem

The CR3BP is often used when modeling the trajectory of spacecraft past GEO orbit. In this dynamical model, the Moon is orbiting the Earth in a perfectly circular orbit. Both the mass of the Earth and Moon influence the motion of the satellite, which is of an assumed negligible mass. This system is often viewed with respect to a synodic reference frame as shown with respect to the inertial reference frame in Fig. 1:

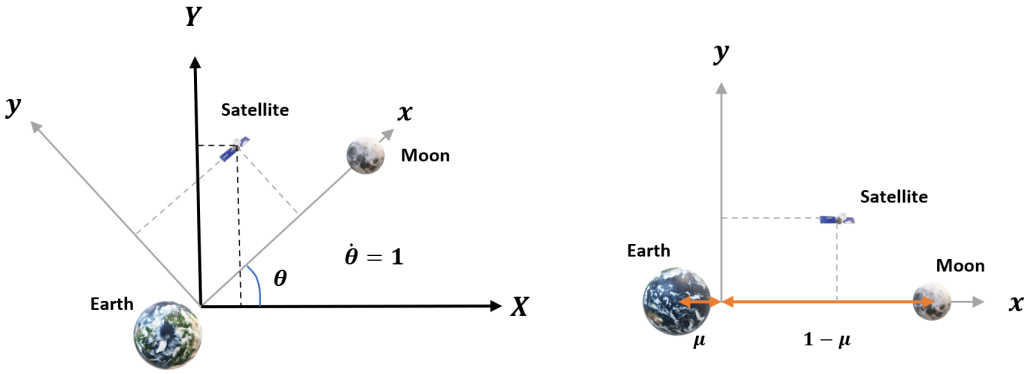

Fig. 1: CR3BP Inertial Reference frame (X,Y) and Synodic Reference Frame (x,y)

In the synodic reference frame the Earth and Moon remain on the x-axis at fixed, non-dimensional distances $-\mu$ and $1-\mu$ respectively. In this analysis, the non-dimensional mass parameter, μ, is equal to 0.012150584673414. The non-dimensional equations of motion are shown in Eq. (1) below:

$$\begin{aligned} \ddot{x} &= x + 2\dot{y} - \frac{(1-\mu)(x+\mu)}{r_{sat/e}^3} - \frac{\mu(x-1+\mu)}{r_{sat/m}^3} \\ \ddot{y} &= y - 2\dot{x} - \frac{(1-\mu)y}{r_{sat/e}^3} - \frac{\mu y}{r_{sat/m}^3} \\ \ddot{z} &= -\frac{(1-\mu)z}{r_{sat/e}^3} - \frac{\mu z}{r_{sat/m}^3} \end{aligned} \tag{1}$$

where the scalar distance of the satellite (*sat*) with respect to the Earth and Moon in the synodic reference frame is written as Eqs. (2) and (3), respectively:

$$r_{sat/e}^2 = (x+\mu)^2 + y^2 + z^2 \tag{2}$$

$$r_{sat/m}^2 = (x-1+\mu)^2 + y^2 + z^2 \tag{3}$$

The variables for distance, time, and mass were non-dimensionalized according to the characteristic quantities given in Table 1. The DU is equal to the distance between the Earth and Moon, the TU is equal to the period of the system divided by a non-dimensional period equal to 2π (i.e. $TU = \frac{P_d}{2\pi}$), and the MU is equal to the sum of the Earth and Moon masses (i.e. $MU = m_e + m_m$). The DU, TU, and MU used in this analysis are provided in Table 1 below:

Table 1: CR3BP Characteristic Quantities

Parameter	Value
Distance Unit (DU)	390,877.4158212686 km
Time Unit (TU)	4.4527 days
Mass Unit (MU)	6.0459×10^{24} kg

Constants used in the CR3BP analysis are shown in Table 2:

Table 2: CR3BP Constants

Parameter	Value
G	$6.674 \times 10^{-20} \frac{Nkm^3}{kg^2}$
m_e	5.9724×10^{24} kg
m_m	7.346×10^{22} kg

3.2 Bicircular Restricted Four-Body Problem

The BCR4BP is developed from the CR3BP, in which the Sun's gravitational effect is included as a perturbation. These effects become noticeable when stable regions in the CR3BP, such as the Lagrange L4 and L5 points, become unstable with the introduction of solar gravitational influences. The system is illustrated below in Fig. 2, with the Sun represented by the capital letter, S:

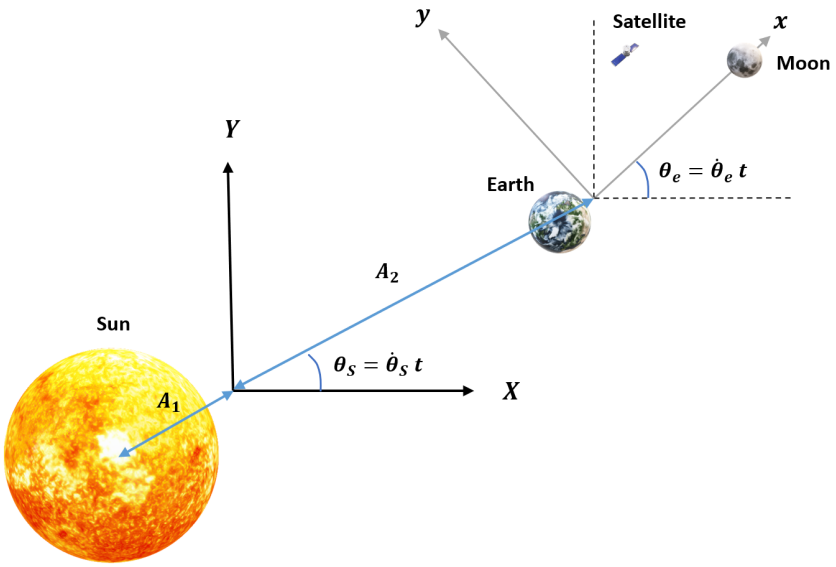

Fig. 2: BCR4BP Inertial Reference frame (X,Y) and Synodic Reference Frame (x,y)

The equations of motion for the BCR4BP are shown in Eq. (4):

$$\begin{aligned}
\ddot{x} &= x + 2\dot{y} - \frac{(1-\mu)(x+\mu)}{r_{sat/e}^3} - \frac{\mu(x-1+\mu)}{r_{sat/m}^3} - \frac{\mu_S(x-x_S)}{r_{sat/S}^3} + A_2\dot{\theta}_S^2\cos(\theta_S-\theta_e) \\
\ddot{y} &= y - 2\dot{x} - \frac{(1-\mu)y}{r_{sat/e}^3} - \frac{\mu y}{r_{sat/m}^3} - \frac{\mu_S(y-y_S)}{r_{sat/S}^3} + A_2\dot{\theta}_S^2\sin(\theta_S-\theta_e) \\
\ddot{z} &= -\frac{(1-\mu)z}{r_{sat/e}^3} - \frac{\mu z}{r_{sat/m}^3} - \frac{\mu_S z}{r_{sat/S}^3}
\end{aligned} \tag{4}$$

where A_1 represents the scalar non-dimensional distance between the Sun and the inertial reference frame, while A_2 represents the scalar non-dimensional distance between the inertial and Earth-Moon synodic reference frames. The scalar distances of the satellite with respect to the Earth, Moon, and Sun in the synodic reference frame (x,y) are written as Eqs. (5), (6), and (7), respectively:

$$r_{sat/e}^2 = (x+\mu)^2 + y^2 + z^2 \tag{5}$$

$$r_{sat/m}^2 = (x-1+\mu)^2 + y^2 + z^2 \tag{6}$$

$$r_{sat/S}^2 = (x-x_S)^2 + (y-y_S)^2 + z^2 \tag{7}$$

where x_S and y_S are the x- and y-coordinates of the Sun with respect to the barycenter of the Earth-Moon synodic reference frame. The equations for x_S and y_S are shown in Eqs (8) and (9), respectively:

$$x_S = -(A_1 + A_2)\cos(\theta_S - \theta_e) \tag{8}$$

$$y_S = -(A_1 + A_2)\sin(\theta_S - \theta_e) \tag{9}$$

and the angles θ_S and θ_e are calculated from Eq. (10) and (11), respectively:

$$\theta_S = \dot{\theta}_S t = \sqrt{\frac{\mu_S + 1}{(A_1 + A_2)^3}}t \tag{10}$$

$$\theta_e = \dot{\theta}_e t = (1)t \tag{11}$$

An important assumption to note in these equations is that at the beginning of propagation, $\theta_S = 0$, however the Sun may be placed at any desired angle by adding the desired starting angle inside the trignometric functions of Eqs. (4), (8), and (9). The BCR4BP uses the same values listed in Tables 1 and 2 with additional quantities listed in Table 3 below:

Table 3: BCR4BP Non-dimensional Constants

Parameter	Value
A_1	0.00116
A_2	382.7275
μ_S	328900
$\dot{\theta}_S$	0.0766

The values in Table 3 are obtained by dividing the scalar distances, times, and masses by the values in Table 1.

3.3 Space Domain Awareness

To determine if the Target satellites in the Lyapunov orbit are visible, visual magnitude (M_v) of the vehicles is calculated. The first step in calculating visual magnitude is to determine the phase (or Sun) angle at every point in time. The phase angle is calculated from Eq. (12):

$$\phi = \arccos\left(\frac{\vec{r}_{Tar/sat} \cdot \vec{r}_{Tar/S}}{r_{Tar/sat} r_{Tar/S}}\right) \tag{12}$$

where $\vec{r}_{Tar/sat}$ is the vector position of the target with respect to the sensor bearing satellite, and $\vec{r}_{Tar/S}$ is the vector position of the target with respect to the Sun. In this analysis, the target is modeled as a sphere; therefore, the phase function, Ψ, becomes:

$$\Psi = \frac{2}{3}\frac{C_d}{\pi}(\sin\phi + (\pi - \phi)\cos\phi) \tag{13}$$

where C_d is the coefficient of diffuse reflection which is a function of the mean wavelength. The visual magnitude, M_v, is then calculated by:

$$M_v = -26.8 - 2.5\log_{10}\left(\frac{A}{r_{Tar/sat}^2}\Psi\right) \tag{14}$$

where A is the surface area of the Target. The visual magnitude is, counterintuitively, measured on a logarithmic scale in which lower numbers indicate brighter objects. For comparison, Table 4 lists common visual magnitudes.

Table 4: Common Visual Magnitudes [10]

Object	M_v
Sun from Earth	-26.8
Full Moon from Earth	-12.5
Jupiter at brightest from Earth	-2.7
Polaris from Earth	1.99
Naked Eye Limit Ability	6
Pluto from Earth	15.1
Hubble Space Telescope Ability	31

For this analysis, a Target is considered visible when it has a visual magnitude of $M_v \leq 18.5$. Constants used in the SDA analysis were area of the Target, A, and coefficient of diffuse reflection, C_d which were 2.25 m^2 and 0.86, respectively. It is critical to note that A is converted to kilometers before calculating M_v to match units of r^2.

Exclusion angles are also considered in this analysis, which are the angles between the satellite-Target and satellite-gravitational body. When the angle between the satellite-Target and satellite-gravitational body vectors are less than these exclusion angles, the target is assumed to be imperceptible due to the Sun's reflection onto the respective gravitational body. Table 5 shows the sun exclusion angles used:

Table 5: Exclusion Angles

Object	Value	M_v
Sun	30°	35
Earth	15°	35
Moon	6°	35

For graphical purposes, high M_v values are assigned to angles which are less than the exclusion angle as shown in Table 5. For instance, a M_v value of 35 would correspond to a scenario in which the Target is imperceptible due to either the Sun, Earth, or Moon's exclusion angle.

3.4 Differential Correction

Differential correction is used to correct a set of initial conditions to satisfy certain criteria. For instance, differential correction is used in targeting problems if a desired final position is specified. Differential correction, in terms of what was used in this work, is also used for transitioning a trajectory between different dynamical model (such as going from the CR3BP to the BCR4BP), or altering initial conditions to account for variations in the attributes of the system (such as a different μ value). The differential correction routines used in this work are outlined by Parker and Anderson [8], and described in detail below.

The differential correction relies on the use of the state transition matrix (STM). The STM, Φ, provides mapping from the initial condition to the final state at a particular time. To begin describing the STM, a state vector $\mathbf{X}$ is defined as Eq. (15)

$$\mathbf{X} = \begin{bmatrix} x & y & z & \dot{x} & \dot{y} & \dot{z} \end{bmatrix} \tag{15}$$

The STM is then,

$$\Phi(t,t_0) = \frac{\partial \mathbf{X}(t)}{\partial \mathbf{X}(t_0)} = \begin{bmatrix} \Phi_{rr} & \Phi_{rv} \\ \Phi_{vr} & \Phi_{vv} \end{bmatrix} \tag{16}$$

and relates the final conditions $\left(\vec{r}(t) \text{ and } \vec{v}(t)\right)$ to the initial conditions $\left(\vec{r}_0 \text{ and } \vec{v}_0)\right)$ conditions by:

$$\begin{bmatrix} \delta\vec{r}(t) \\ \delta\vec{v}(t) \end{bmatrix} = \begin{bmatrix} \Phi_{rr} & \Phi_{rv} \\ \Phi_{vr} & \Phi_{vv} \end{bmatrix} \begin{bmatrix} \delta\vec{r}_0 \\ \delta\vec{v}_0 \end{bmatrix} \tag{17}$$

in which Φ_{rr}, Φ_{rv}, Φ_{vr}, and Φ_{vv} are $3x3$ sub-matrices which comprise the $6x6$ STM. Note that the STM directly maps the deviations or errors in the state. In order to solve for the STM which maps $\mathbf{X}(t)$ to $\mathbf{X}(t_0)$, the STM is propagated for time t via the relationship in Eq. (18):

$$\dot{\Phi}(t,t_0) = A(t)\Phi(t,t_0) \tag{18}$$

where the initial condition for Φ is the identity martix as shown in Eq. 19:

$$\Phi(t_0,t_0) = I = \begin{bmatrix} 1 & 0 & 0 & 0 & 0 & 0 \\ 0 & 1 & 0 & 0 & 0 & 0 \\ 0 & 0 & 1 & 0 & 0 & 0 \\ 0 & 0 & 0 & 1 & 0 & 0 \\ 0 & 0 & 0 & 0 & 1 & 0 \\ 0 & 0 & 0 & 0 & 0 & 1 \end{bmatrix} \tag{19}$$

The A Matrix in Eq. (18) is solved by evaluating Eq. (20):

$$A(t) = \frac{\partial\dot{\mathbf{X}}(t)}{\partial\mathbf{X}(t)} = \begin{bmatrix} a_{11} & a_{12} \\ a_{21} & a_{22} \end{bmatrix} \tag{20}$$

where

$$a_{11} = \begin{bmatrix} \frac{\partial\dot{x}}{\partial x} & \frac{\partial\dot{x}}{\partial y} & \frac{\partial\dot{x}}{\partial z} \\ \frac{\partial\dot{y}}{\partial x} & \frac{\partial\dot{y}}{\partial y} & \frac{\partial\dot{y}}{\partial z} \\ \frac{\partial\dot{z}}{\partial x} & \frac{\partial\dot{z}}{\partial y} & \frac{\partial\dot{z}}{\partial z} \end{bmatrix} \qquad a_{12} = \begin{bmatrix} \frac{\partial\dot{x}}{\partial\dot{x}} & \frac{\partial\dot{x}}{\partial\dot{y}} & \frac{\partial\dot{x}}{\partial\dot{z}} \\ \frac{\partial\dot{y}}{\partial\dot{x}} & \frac{\partial\dot{y}}{\partial\dot{y}} & \frac{\partial\dot{y}}{\partial\dot{z}} \\ \frac{\partial\dot{z}}{\partial\dot{x}} & \frac{\partial\dot{z}}{\partial\dot{y}} & \frac{\partial\dot{z}}{\partial\dot{z}} \end{bmatrix}$$

$$a_{21} = \begin{bmatrix} \frac{\partial\ddot{x}}{\partial x} & \frac{\partial\ddot{x}}{\partial y} & \frac{\partial\ddot{x}}{\partial z} \\ \frac{\partial\ddot{y}}{\partial x} & \frac{\partial\ddot{y}}{\partial y} & \frac{\partial\ddot{y}}{\partial z} \\ \frac{\partial\ddot{z}}{\partial x} & \frac{\partial\ddot{z}}{\partial y} & \frac{\partial\ddot{z}}{\partial z} \end{bmatrix} \qquad a_{22} = \begin{bmatrix} \frac{\partial\ddot{x}}{\partial\dot{x}} & \frac{\partial\ddot{x}}{\partial\dot{y}} & \frac{\partial\ddot{x}}{\partial\dot{z}} \\ \frac{\partial\ddot{y}}{\partial\dot{x}} & \frac{\partial\ddot{y}}{\partial\dot{y}} & \frac{\partial\ddot{y}}{\partial\dot{z}} \\ \frac{\partial\ddot{z}}{\partial\dot{x}} & \frac{\partial\ddot{z}}{\partial\dot{y}} & \frac{\partial\ddot{z}}{\partial\dot{z}} \end{bmatrix}$$

There are certain properties which the Φ matrix possess which are described below:

$$\Phi(t_2,t_0) = \Phi(t_2,t_1)\Phi(t_1,t_0) \tag{21}$$

$$\Phi^{-1}(t,t_0) = \Phi(t_0,t) \tag{22}$$

With knowledge of the STM, differential correction may be performed via the single and multiple shooting methods. For both methods, a set number of patchpoints are chosen which allows for convergence of the algorithm outlined in Fig. 3. The first step in differential correction is the single shooting method. In the Single Shooting method the patchpoint positions and times to travel between patchpoints are held constant whilst the velocity is varied to a converged solution as to reach a desired position in a desired amount of time. It is crucial that the initial velocity guess is close to the solution or else the velocity will not converge. Likewise, orbital dynamics in cislunar periodic orbits are extremely chaotic, thus it is important to impose enough patchpoints as to allow for a converged solution (especially around sharp "turns" in the trajectory). The algorithm for utilizing this single shooting method is shown in Fig. 3:

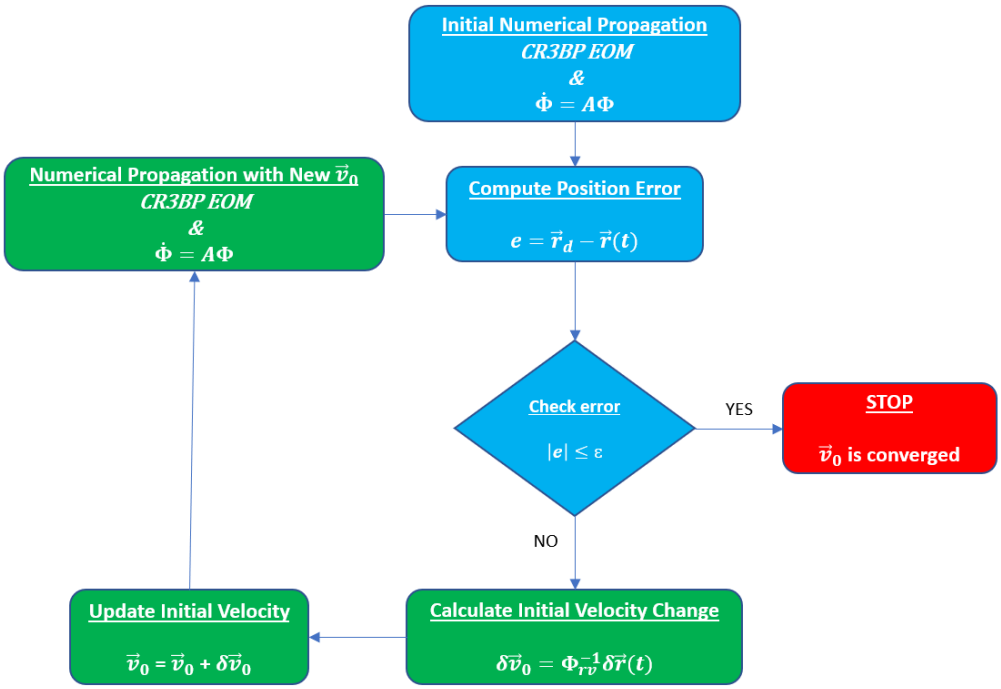

Fig. 3: Single Shooting Method Algorithm

In the preceding algorithm, ε is the error tolerance, $\vec{r}_d$ is the desired position, and the equation for the initial velocity change is calculated from Eq. (17) and shown in Eq. (23):

$$\delta\vec{v}_0 = \Phi_{rv}^{-1}\delta\vec{r}(t) \tag{23}$$

If using the single shooting method for multiple points in a trajectory, then it is critical to remember to propagate each respective point at the start time in the overall trajectory, as opposed to starting each point at t = 0.

The multiple shooting method is used after the single shooting method to adjust position and times. The change in patchpoint position and times for a three-pathchpoint segment is calculated from Eq. (24):

$$\begin{bmatrix} \delta R_1 \\ \delta t_1 \\ \delta R_2 \\ \delta t_2 \\ \delta R_3 \\ \delta t_3 \end{bmatrix} = M^T (MM^T)^{-1} \left[\delta \Delta V_2\right] \tag{24}$$

The goal with Eq. (24) is to reduce ΔV_2 to zero. Note that $\Delta V_2 = V_2^+ - V_2^-$ where the the solo superscripts "-" and "+" represent the incoming and outgoing parameters at a particular patchpoint. The M matrix is calculated by Eq. (25):

$$M = \begin{bmatrix} \frac{\partial \Delta V_2}{\partial R_1} & \frac{\partial \Delta V_2}{\partial t_1} & \frac{\partial \Delta V_2}{\partial R_2} & \frac{\delta \partial V_2}{\partial t_2} & \frac{\partial \Delta V_2}{\partial R_3} & \frac{\partial \Delta V_2}{\partial t_3} \end{bmatrix} \tag{25}$$

Where

$$\frac{\partial \Delta V_2}{\partial R_1} = -\frac{\partial V_2^-}{\partial R_1^+} = -B_{12}^{-1} \qquad \frac{\partial \Delta V_2}{\partial t_2} = \frac{\partial V_2^+}{\partial t_2^-} - \frac{\partial V_2^-}{\partial t_2^+} = B_{32}^{-1} A_{32} V_2^+ - B_{12}^{-1} A_{12} V_2^-$$

$$\frac{\partial \Delta V_2}{\partial t_1} = -\frac{\partial V_2^-}{\partial t_1^+} = B_{12}^{-1} V_1^+ \qquad \frac{\partial \Delta V_2}{\partial R_3} = \frac{\partial V_2^+}{\partial R_3^-} = B_{32}^{-1}$$

$$\frac{\partial \Delta V_2}{\partial R_2} = -\frac{\partial V_2^+}{\partial R_2^-} - \frac{\partial V_2^-}{\partial R_2^+} = -B_{32}^{-1} A_{32} + B_{12}^{-1} A_{12} \qquad \frac{\partial \Delta V_2}{\partial t_3} = \frac{\partial V_2^+}{\partial t_3^-} = -B_{32}^{-1} V_3^-$$

which utilizes the notation in Eq. (26):

$$\begin{bmatrix} \delta R_2^- \\ \delta V_2^- \end{bmatrix} = \begin{bmatrix} A_{21} & B_{21} \\ C_{21} & D_{21} \end{bmatrix} \begin{bmatrix} \Delta R_1^+ \\ \Delta V_1^+ \end{bmatrix} \tag{26}$$

where the A_{21}, B_{21}, C_{21} and D_{21} sub-matrices form the STM mapping from patchpoint 1 to 2. Finally, to determine the new positions add the variation in position obtained to the initial position as shown in Eqs. (27) and (28):

$$\vec{r}_{1new} = \vec{r}_{1old}^{+} + \delta \vec{r}_1 \tag{27}$$

$$\vec{r}_{2new} = \vec{r}_{2old}^{-} + \delta \vec{r}_2 \tag{28}$$

This process describes the multiple shooting method for 3 points; for more than 3 points, then a matrix form shown in Eq. (29) may be used:

$$\begin{bmatrix} \delta R_1 \\ \delta t_1 \\ \delta R_2 \\ \delta t_2 \\ \delta R_3 \\ \delta t_3 \\ \delta R_4 \\ \delta t_4 \\ \vdots \\ \delta R_n \\ \delta t_n \end{bmatrix} = M^T (M M^T)^{-1} \begin{bmatrix} \delta \Delta V_2 \\ \delta \Delta V_3 \\ \vdots \\ \delta \Delta V_{n-1} \end{bmatrix} \tag{29}$$

From Eq. (29), the matrix M is equal to

$$M = \begin{bmatrix} \frac{\partial \Delta V_2}{\partial R_1} & \frac{\partial \Delta V_2}{\partial t_1} & \frac{\partial \Delta V_2}{\partial R_2} & \frac{\partial \Delta V_2}{\partial t_2} & \frac{\partial \Delta V_2}{\partial R_3} & \frac{\partial \Delta V_2}{\partial t_3} & 0_{3x3} & 0_{3x1} & \dots & 0_{3x3} & 0_{3x1} \\ 0_{3x3} & 0_{3x1} & \frac{\partial \Delta V_3}{\partial R_2} & \frac{\partial \Delta V_3}{\partial t_2} & \frac{\partial \Delta V_3}{\partial R_3} & \frac{\partial \Delta V_3}{\partial t_3} & \frac{\partial \Delta V_3}{\partial R_4} & \frac{\partial \Delta V_3}{\partial t_4} & \dots & 0_{3x3} & 0_{3x1} \\ \vdots & \vdots & \vdots & \vdots & \vdots & \vdots & \vdots & \vdots & \vdots & \vdots & \vdots \\ 0_{3x3} & 0_{3x1} & 0_{3x3} & 0_{3x1} & \dots & \frac{\partial \Delta V_{n-1}}{\partial R_{n-2}} & \frac{\partial \Delta V_{n-1}}{\partial t_{n-2}} & \frac{\partial \Delta V_{n-1}}{\partial R_{n-1}} & \frac{\partial \Delta V_{n-1}}{\partial t_{n-1}} & \frac{\partial \Delta V_{n-1}}{\partial R_n} & \frac{\partial \Delta V_{n-1}}{\partial t_n} \end{bmatrix} \tag{30}$$

where 0_{3x3} is a 3x3 matrix of zeros and 0_{3x1} is a 3x1 matrix of zeros. For correcting the position, the following is used:

$$\vec{r}_{n-new} = \vec{r}_{n-old}^{+} + \delta \vec{r}_n \tag{31}$$

4. ANALYSIS AND RESULTS

In performing the SDA simulations, Systems Tool Kit (STK) was utilized to model the sensors and dynamics [6]. Data was extracted from the simulation and plotted for analysis.

4.1 Cislunar Periodic Orbits

The starting initial conditions of the periodic orbits used in this work were obtained through the works of Arenstorf [1, 2] who used a dated μ value (μ = 0.012277471) that was accurate to the available data of the 1960's. However, with technological advancements, the modern accepted Earth-Moon μ value is slightly different than what Arenstorf and his contemporaries used, and is closer to $\mu = 0.01215$. The starting initial conditions of the target Lyapunov orbit was obtained through the works of Grebow [5], who used a μ value of $\mu = 0.0121505856$. It is important to note, however, that Grebow only provided 4 digits of precision in their y-velocity initial condition, thus making the orbit slightly non-periodic. This numerical deviation was corrected for when transitioning the orbit to the standardized μ value used in this work ($\mu = 0.012150584673414$). The starting initial conditions with original μ values for all three periodic orbits and the Target Lyapunov orbit analyzed herein are shown in Table 6:

Table 6: Pre-Corrected Periodic Orbit Initial Conditions in CR3BP

Parameter	Orbit 1	Orbit 2	Orbit 3	Target Lyapunov Orbit
x_0	0.994	0.994	0.9765	0.7589
y_0	0	0	0	0
z_0	0	0	0	0
$\dot{x}_0$	0	0	0	0
$\dot{y}_0$	-2.113898796694	-2.031732629557	-1.690574108489	0.5068
$\dot{z}_0$	0	0	0	0
T_0	5.4368	11.1243	12.3287	4.6052

The values in Table 6 were corrected for a modern μ value using differential correction with 21 patchpoints combined with trial and error of changing the initial y-velocity to ensure periodicity for at least two periods on each orbit of the periodic orbits. The Lyapunov orbit was correct via correcting the initial y-velocity through trial and error until at periodicity was ensured for at least three periods. The corrected initial conditions for each periodic orbit in the CR3BP are shown in Table 7:

Table 7: Corrected Periodic Orbit Initial Conditions in CR3BP

Parameter	Orbit 1	Orbit 2	Orbit 3	Target Lyapunov Orbit
μ	0.012150584673414	0.012150584673414	0.012150584673414	0.012150584673414
x_0	0.993999897750721	0.994000000062232	0.976500014687630	0.7589
y_0	-3.7306354×10^{-8}	$-2.123829160152473\times10^{-9}$	0	0
z_0	0	$-1.936516349916483\times10^{-9}$	-1.6769213×10^{-8}	0
$\dot{x}_0$	0.003741232665221	0.001967678410973	0.008008641313757	0
$\dot{y}_0$	-2.122884103965	-2.0413426475	-1.6768357651	0.5067417734466
$\dot{z}_0$	0	$-1.169055050872915\times10^{-6}$	0	0
T_0	5.4368	11.1243	12.3287	4.6052

The periodic orbit initial conditions shown in Table 7 are corrected to allow at least two full repeating periods where no propellant would be required in the CR3BP. The Lyapunov orbit initial conditions are corrected to allow at least three full repeating periods where no propellant would be required in the CR3BP. This was to allow for the scenario to play out in STK without risk of divergent trajectories. Plotting the initial conditions from Table 7 provides the orbits in Fig. 4:

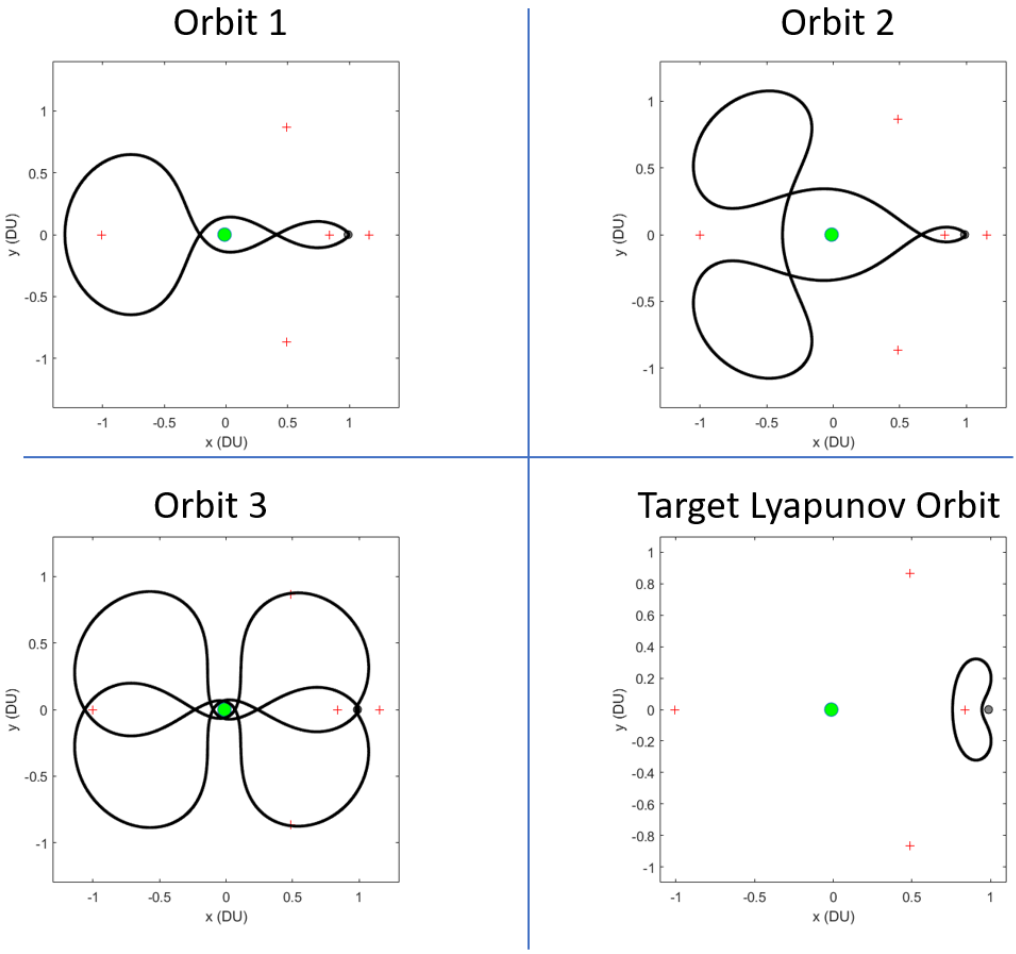

Fig. 4: Periodic Orbits and Target Lyapunov Orbit

4.2 Simulation

In this analysis STK's Astrogator system was used to perform all three simulations. While all orbits were propagated in a Earth-Moon CR3BP model within STK, Sun exclusion angles were also considered with the Sun located by a realistic ephemeris model which is built into STK. The start date and time for all simulations was 28 Mar 2021 at 1600 UTCG. The vector range data during the simulations was obtained in 30 minute intervals.

An efficient way of comparing the effectiveness of each periodic orbit is to reduce as many differences between the scenarios as possible. In reducing free variables between scenarios, the same number of sensor satellites and Targets were chosen for each periodic orbit scenario. For each scenario, 2 Targets were chosen to be traversing the L1 Lyapunov trajectory with 10 sensor bearing satellites orbiting the periodic orbit. Each periodic orbit scenario was propagated for 12.3287 TU as to allow at least one full period for each scenario. Recording data in 30 minute intervals provided for 5272 time steps of data throughout the scenario. The result of the scenario containing 10 sensor bearing satellites monitoring 2 Targets each and 5272 time steps is that there are 105440 "instances" in which data is recorded. Since there are 2 Targets, there were 52720 "instances" of data per Target. Both the sensor satellites and Targets were spaced out evenly in time in their respective constellation.

For the first scenario containing Orbit 1, the results are shown in Fig. 5:

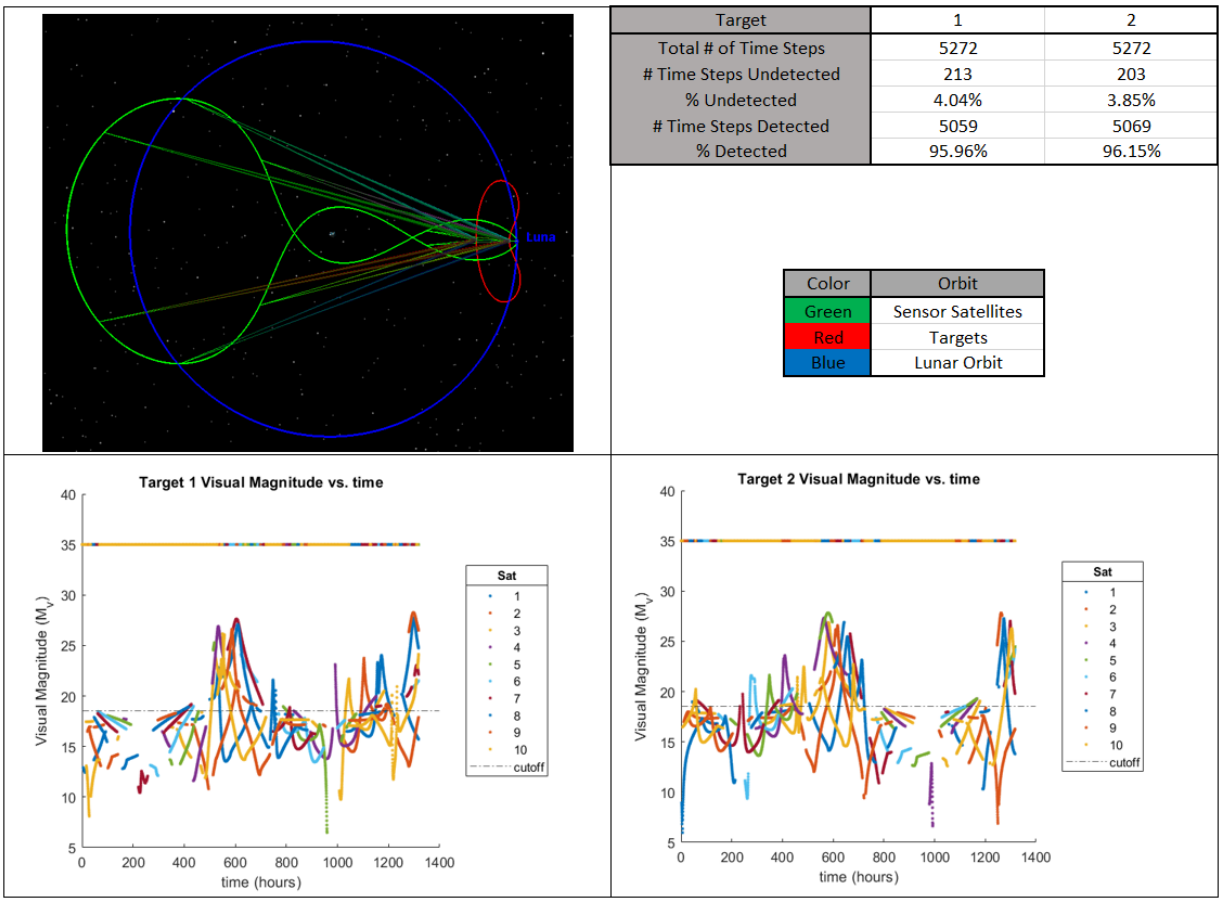

Target	1	2
Total # of Time Steps	5272	5272
# Time Steps Undetected	213	203
% Undetected	4.04%	3.85%
# Time Steps Detected	5059	5069
% Detected	95.96%	96.15%

Color	Orbit
Green	Sensor Satellites
Red	Targets
Blue	Lunar Orbit

Fig. 5: Scenario 1 Simulation and Results

For Scenario 1, there were 213 of 5272 time steps in which none of the 10 sensor satellites were able to view Target 1, either due to a M_v greater than the cutoff of 18.5 or due to an exclusion angle of the Sun, Earth, or Moon. This resulted in Target 1 being visible 95.96% of the simulation by at least one satellite. Likewise, there were 203 of 5272 time steps in which none of the 10 sensor satellites were able to view Target 2, either due to a M_v greater than the cutoff of 18.5 or due to an exclusion angle of the Sun, Earth, or Moon. This resulted in Target 2 being visible 96.15% of the simulation by at least one satellite.

The results of the exclusion angle data showed that for Target 1 the Sun, Earth, and Moon caused the satellite to be imperceptible 10545, 18369, and 15764 of 52720 instances respectively; for Target 2, the Sun, Earth, and Moon caused the satellite to be imperceptible 10476, 18649, and 15172 of 52720 instances. It is important to note that one instance could include multiple exclusion angles. These results showed that for Orbit 1, the Earth has the largest impact in terms of exclusion angles. This is logical due to the long and close proximity passes with respect to the Earth.

Orbit 1 is the simplest periodic orbit hosting the shortest period in this work. This is beneficial in reducing the total number of satellites needed to perform cislunar SDA. It was originally expected, however, that this orbit would not perform as well as demonstrated herein for monitoring a Lyapunov orbit due to Earth exclusion angles caused by close proximity Earth passes. In reality, the satellites along this trajectory pass the Earth extremely quick when compared to the path on the lunar opposing side of the Earth. This, combined with the increased frequency of the satellites being in close proximity of the Lyapunov orbit, creates a high percentage of detection time.

The results of the second scenario containing Orbit 2 are shown in Fig. 6:

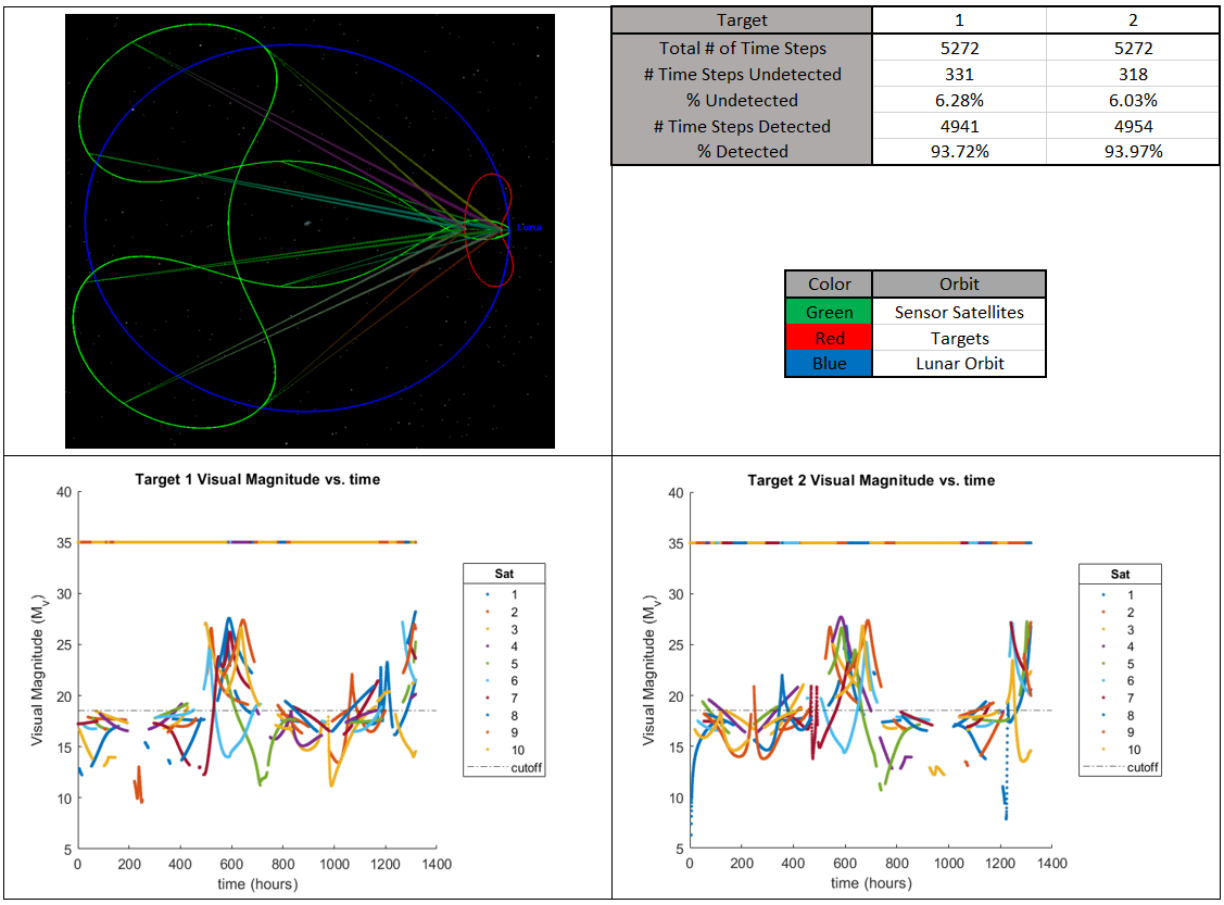

Target	1	2
Total # of Time Steps	5272	5272
# Time Steps Undetected	331	318
% Undetected	6.28%	6.03%
# Time Steps Detected	4941	4954
% Detected	93.72%	93.97%

Color	Orbit
Green	Sensor Satellites
Red	Targets
Blue	Lunar Orbit

Fig. 6: Scenario 2 Simulation and Results

For Scenario 2, Target 1 was visible 93.72% of the simulation by at least one satellite while Target 2 was visible 93.97% of the simulation by at least one satellite. Compared to Orbit 1, Targete 1 and 2 were observed for 2.24% and 2.18% less of the simulation time respectively in Orbit 2.

The results of the exclusion angle data showed that for Target 1 the Sun, Earth, and Moon caused the satellite to be imperceptible 10039, 12805, and 17404 of 52720 instances, respectively. For Target 2, the Sun, Earth, and Moon caused the satellite to be imperceptible 9882, 12971, and 17040 of 52720 instances. These results showed that for Orbit 2, the Moon has the largest impact in terms of exclusion angles. The reason for this is thought to be due to the large gap in the orbit with respect to the Earth and the large portion of the trajectory which is located on the opposite side of the Earth than the Target.

Orbit 2 had the lowest percentage of detections of Targets 1 and 2, making it the lowest performer in this simulation. Compared to Orbit 1, Orbit 2 has an additional loop on the opposite side of the Earth with respect to the Target. This increases the portion of the trajectory path of Orbit 2 that allows for Earth exclusion angle imperceptibility. While the tops and bottoms of these loops cause Earth exclusion angles to be a non-issue, at these locations the sensors are so far away from the Targets that there is an increased risk of the visual magnitude being above the cutoff. Therefore, it is reasonable that there are less time steps in which the Targets are visible by at least one satellite.

The results of the third scenario containing Orbit 3 are shown in Fig. 7:

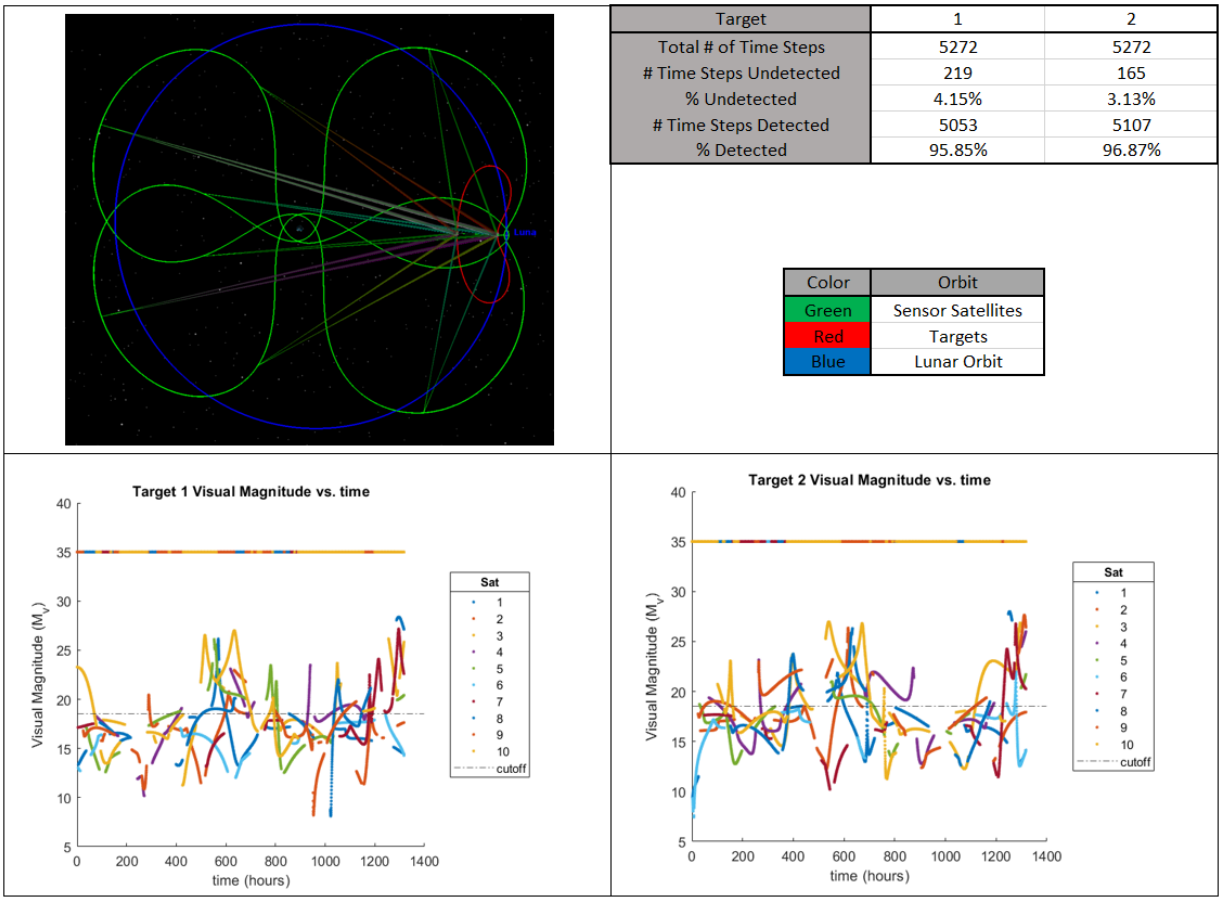

Target	1	2
Total # of Time Steps	5272	5272
# Time Steps Undetected	219	165
% Undetected	4.15%	3.13%
# Time Steps Detected	5053	5107
% Detected	95.85%	96.87%

Color	Orbit
Green	Sensor Satellites
Red	Targets
Blue	Lunar Orbit

Fig. 7: Scenario 3 Simulation and Results

For Scenario 3, Target 1 was visible 95.85% of the simulation by at least one satellite while Target 2 was visible 96.87% of the simulation by at least one satellite. These results are comparable to Orbit 1, with Orbit 3 showing a slight decrease in detection of Target 1 by 0.11% coupled with a minor decrease in detection of Target 2 by 0.72%.

The results of the exclusion angle data showed that, for Target 1 the Sun, Earth, and Moon caused the satellite to be imperceptible 9870, 13169, and 17051 of 52720 instances, respectively. Similarly, for Target 2, the Sun, Earth, and Moon caused the satellite to be imperceptible 10124, 13270, and 16199 of 52720 instances. These results showed that for Orbit 3, the Moon has the largest impact in terms of exclusion angles. This is logical due half of the trajectory being out of the realm of possibility for an Earth exclusion angle imperceptibility.

Orbit 3 performed less than one percentage point worse in monitoring Target 1 and less than one percentage point better in monitoring Target 2 than Orbit 1. The large loops which are located on the same side of the Earth as the Moon provide for a high probability of viewing the Targets with no risk of issues caused by Earth exclusion angles and minimal risk of issues from lunar exclusion angles.

4.3 BCR4BP ΔV Analysis

Propellant expenditure, commonly referred to as ΔV, is a dominant cost in orbital dynamics. While the orbits analyzed in this work are periodic in the CR3BP, potentially requiring no ΔV, these orbits become more chaotic when subject to higher fidelity models such as the BCR4BP. Therefore, this section addresses this issue and determines the approximate ΔV which would be required to maintain these orbits for one period. The methodology for determining the ΔV needed to maintain periodicity is using the initial conditions found in Table 6 to create patchpoints then using the single shooting method to update the velocities in the BCR4BP. The total ΔV is calculated as the sum of the individual ΔV's at each of the 19 middle patchpoints. This was performed on four different starting angles for the Sun with respect

to the synodic reference frame x-axis for each orbit, however, all of the patchpoint $\Delta V's$ are shown for an initial Sun starting angle of 0° in Table 8 as an example. To assist in visualisation, the trajectories between patchpoints for all 3 orbits are shown in Fig. 8. The results of this analysis are presented in Table 9 with the ΔV in units of meters/second calculated for one period of each orbit:

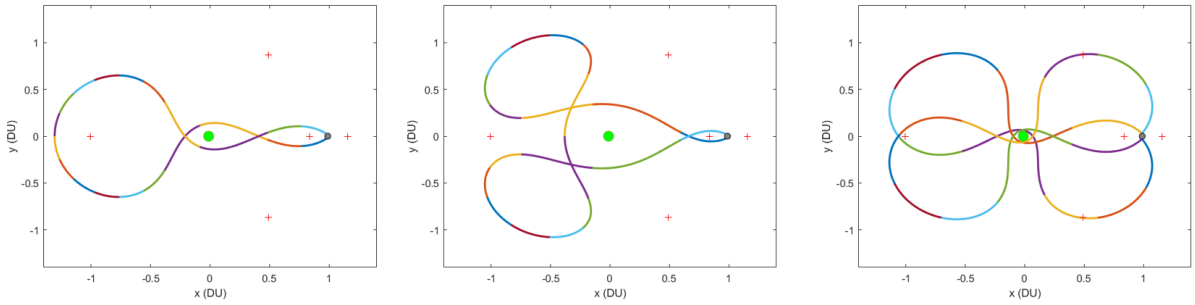

Fig. 8: Periodic Orbits Subject to the Single Shooting Method in BCR4BP

Table 8: Approximate ΔV required per patchpoint in to Maintain Orbit in 0° Initial Sun Position BCR4BP (in m/s)

patchpoint	Orbit 1 ΔV	Orbit 2 ΔV	Orbit 3 ΔV
2	5.8589×10^{-5}	9.0397×10^{-4}	1.5985×10^{-5}
3	2.3138×10^{-5}	0.0034	5.904×10^{-4}
4	0.0031	4.6343×10^{-4}	0.0012
5	0.0018	1.0069×10^{-4}	3.0084×10^{-8}
6	3.6562×10^{-6}	6.6899×10^{-5}	6.1955×10^{-4}
7	4.5143×10^{-6}	8.3479×10^{-5}	5.3685×10^{-4}
8	3.7325×10^{-6}	8.4996×10^{-5}	7.2924×10^{-4}
9	3.0385×10^{-6}	2.3968×10^{-4}	0.0015
10	2.6179×10^{-6}	8.6959×10^{-4}	1.2701×10^{-8}
11	2.6411×10^{-6}	7.5576×10^{-4}	4.1062×10^{-4}
12	3.3033×10^{-6}	0.0012	8.8575×10^{-8}
13	4.4056×10^{-6}	1.2599×10^{-4}	0.0028
14	6.4036×10^{-6}	9.3047×10^{-5}	1.0913×10^{-4}
15	1.0519×10^{-5}	7.0595×10^{-5}	1.3567×10^{-4}
16	2.0938×10^{-5}	6.939×10^{-5}	2.0492×10^{-4}
17	5.8126×10^{-5}	1.0227×10^{-4}	7.0277×10^{-4}
18	0.0011	2.6977×10^{-4}	0.0024
19	1.3547×10^{-4}	2.1081×10^{-9}	1.9507×10^{-4}
20	1.7924×10^{-5}	2.211×10^{-4}	1.2350×10^{-4}

Table 9: Approximate ΔV per Period Required to Maintain Orbit in BCR4BP (in m/s)

Initial Sun Position	Orbit 1 ΔV	Orbit 2 ΔV	Orbit 3 ΔV
0°	0.0064	0.0091	0.0123
90°	0.0040	0.0060	0.0080
180°	0.0065	0.0091	0.0124
270°	0.0040	0.0059	0.0079
Average	0.0052	0.0075	0.0102

At first glance of Table 9 it appears that Orbit 1 is the most efficient in terms of propellant cost. However, this is to be expected because it hosts the shortest period. To more accurately compare the different periodic orbits, it is beneficial to calculate the unit ΔV each orbit requires, that is, the average ΔV required per one time unit. To accomplish this, the

averages of Table 9 were divided by their respective orbit's non-dimensional period. This obtained the unit ΔV's for orbits 1, 2, and 3 to be 0.000956 $^{m}/_{s}$, 0.000674 $^{m}/_{s}$, and 0.000827 $^{m}/_{s}$ respectively. Therefore, in reality Orbit 2 is the most efficient while Orbit 1 is the least efficient in terms of propellant expenditure required to maintain trajectory per unit of time. This is to be expected since Orbit 1 has the most frequent passes of both the Earth and Moon while Orbit 2 has the least frequent passes. Orbit 2's trajectory is also the furthest from the Earth in terms of flyby distance which, assuming a phase angle which allows for visibility, causes the lowest perturbation effect due to the Earth.

4.4 Recommendations

Orbits 1 and 3 provided similar results for the SDA simulation in terms of how often Targets 1 and 2 were visible. Both of these orbits were able to view the Targets approximately 2-3% of the time more than Orbit 2. In this regard, Orbits 1 and 3 tie as the most effective periodic orbits surveyed in this work for cislunar SDA. However, this is assuming an ideal CR3BP dynamics scenario. In reality, there are many more perturbations which the satellites will experience that will induce chaos and disturb the satellites from their periodic trajectories. Therefore, BCR4BP ΔV analysis was performed to calculate the approximate ΔV which would be required to maintain these trajectories in a higher fidelity model. Solving for the ΔV required per time unit in the BCR4BP showed that Orbit 3 had a lower required propellant expenditure per time unit than Orbit 1. Thus, due to the similarities in detection ability coupled with Orbit 3 being slightly better in terms of propellant expenditure, Orbit 3 is recommended as the most effective surveyed periodic orbit for this cislunar SDA mission architecture.

5. CONCLUSION

Recent developments and planned projects in the space community have caused a revitalization in space travel efforts. With various countries now looking to expand their infrastructure in space, safe space traffic management and monitoring is vital for the continued protection of U.S. assets. The periodic orbits analyzed in this work are an ideal candidate for cislunar SDA mission architectures due to their periodicity, low propellant costs, and ability to traverse a wide expansion of cislunar space. This work sought to present and compare of the effectiveness of three different periodic orbits when subject to the SDA mission architecture of monitoring Targets in a Lyapunov L1 orbit. All initial conditions required adjustments for variations in μ value. The Lyapunov orbit initial conditions also required adjustment due to lack of precision. These orbits were then subject to a simulation in which the visual magnitude was recorded with Sun, Earth, and Moon exclusion angles also considered. Orbits 1 and 3 proved the most effective in this regard, providing similar results. The ΔV required to maintain the periodic orbit trajectories in a higher fidelity BCR4BP was then calculated showing that Orbit 2 had the lowest ΔV per time unit required, followed by Orbit 3 and then Orbit 1. Considering the analysis conducted, Orbit 3 provides for an extremely effective and relatively low cost solution to this cislunar SDA mission architecture.

When compared to the results of a recent study examining lunar-based SDA[4], the periodic orbits in this work had significantly higher viewing rates at the $M_v \leq 18.5$ threshold. The results of this work show promise of exploiting periodic orbits for future SDA mission architectures. Possible applications include monitoring cislunar notional satellites or space debris for effective space traffic management, resulting in the protection and survival of U.S. space-based assets.

6. REFERENCES

[1] Richard F. Arenstorf. Existence of periodic solutions passing near both masses of the restricted three-body problem. *AIAA Journal*, 1:238–240, 1963.

[2] Richard F. Arenstorf. Periodic trajectories passing near both masses of the restricted three-body problem. *Proceedings of the XIV International Astronautical Congress*, pages 85–97, 1963.

[3] V. A. Egorov. Certain problems of moon flight dynamics. *The Russian Literature of Satellites*, pages 107–174, 1958.

[4] C. Frueh, K. Howell, K.J. DeMars, S. Bhadauria, and M. Gupta. Cislunar space traffic management: Surveillance through earth-moon resonance orbits. *8th European Conference on Space Debris*, 2021.

[5] Daniel J. Grebow. Generating periodic orbits in the circular restricted three-body problem with applications to lunar south pole coverage. 2006.

[6] Systems Tool Kit. Astrogator: Circular restricted three-body problem (cr3bp) configuration, 2021.

[7] K. E. Papadakis. Families of asymmetric periodic orbits in the restricted three-body problem. *Earth, Moon, and Planets*, pages 25–42, 2008.
[8] Jeffery S. Parker and Rodney L. Anderson. *Low-Energy Lunar Trajectory Design*. John Wiley Sons Inc., 2014.
[9] H. Poincaré. *Les Méthodes Nouvelles de la Mécanique Céleste*. Gauthier-Villars, Paris, 1892-1899.
[10] Michael A. Seeds and Dana E. Backman. *The Solar System*, volume 7. CENGAGE Learning, 1997.
[11] Ellis Strömgren. Symmetrische und unsymmetrische librationsähnliche bahnen im probléme restreint mit asymptotisch-peridischen bahnen als grenzbahnen. 1934.
[12] Victor Szebehely. *Theory of Orbits*. Academic Press, 1967.